Design of optimal light delivery system for co-registered transvaginal ultrasound and photoacoustic imaging of ovarian tissue

Hassan S. Salehi [a], Patrick D. Kumavor [b], Hai Li [a], Umar Alqasemi [b], Tianheng Wang [a], Chen Xu [a,b], Quing Zhu [a,b,*]

[a] Department of Electrical and Computer Engineering, University of Connecticut, Storrs, CT 06269, USA
[b] Department of Biomedical Engineering, University of Connecticut, Storrs, CT 06269, USA

ABSTRACT

A hand-held transvaginal probe suitable for co-registered photoacoustic and ultrasound imaging of ovarian tissue was designed and evaluated. The imaging probe consists of an ultrasound transducer and four 1-mm-core multi-mode optical fibers both housed in a custom-made sheath. The probe was optimized for the highest light delivery output and best beam uniformity on tissue surface, by simulating the light fluence and power output for different design parameters. The laser fluence profiles were experimentally measured through chicken breast tissue and calibrated intralipid solution at various imaging depths. Polyethylene tubing filled with rat blood mimicking a blood vessel was successfully imaged up to ~30 mm depth through porcine vaginal tissue at 750 nm. This imaging depth was achieved with a laser fluence on the tissue surface of 20 mJ/cm^2, which is below the maximum permissible exposure (MPE) of 25 mJ/cm^2 recommended by the American National Standards Institute (ANSI). Furthermore, the probe imaging capability was verified with *ex vivo* imaging of benign and malignant human ovaries. The co-registered images clearly showed different vasculature distributions on the surface of the benign cyst and the malignant ovary. These results suggest that our imaging system has the clinical potential for *in vivo* imaging and characterization of ovarian tissues.

1. Introduction

Ovarian cancer has the highest mortality rate of all gynecologic cancers, and is estimated to be the ninth most common cancer and the fifth leading cause of death among all cancers in the United States [1,2]. The lifetime risk of invasive ovarian cancer is approximately 1.4% (1 in 71) and the lifetime risk of death is about 1 in 95 [1]. More than two thirds of ovarian cancer cases are diagnosed in stages III or IV with invasion to the peritoneum and other organs due to nonspecific associated symptoms as well as lack of efficacious screening techniques at the disposal of patients [1–3]. The 5-year survival rate is 94% at the local stage (stage I), while only 15% of ovarian tumors are diagnosed at this stage. This is in sharp contrast to a rate of approximately 28% at the distant stage (stage IV), where 62% of the cases are diagnosed [2]. Unfortunately, there is no simple and reliable way to screen for ovarian cancer. For instance, tumor marker CA 125 along with transvaginal ultrasound (US) yield low positive predictive values (PPVs) of 40% [4–8]. Transvaginal ultrasound alone suffers from a low positive predictive value of 14.1% according to a study done on the annual screening of 25,327 women [9]. Therefore, there is an urgent need to improve the current diagnostic techniques and consequently increase the effectiveness of ovarian cancer screening.

Photoacoustic tomography (PAT) is an emerging imaging modality with great potential to assist transvaginal ultrasound for ovarian cancer screening. In PAT imaging, a short-pulsed laser beam penetrates into biological tissue diffusively. Due to tissue thermoelastic expansion resulting from a transient temperature rise caused by the laser irradiation, the photoacoustic waves are generated and measured by wideband ultrasound transducers [10–22]. The photoacoustic waves are utilized to reconstruct, at ultrasound resolution, the optical absorption distribution that reveals tissue optical contrast. Optical absorption is directly related to neovascularization associated with tumor angiogenesis and hypoxia. Tumor angiogenesis and oxygen consumption are significant factors promoting tumor growth and metastasis [23].

Several optical fiber-based photoacoustic imaging probes have been designed for various applications by several research groups

* Corresponding author. Departments of Electrical and Computer Engineering and Departments of Biomedical Engineering, University of Connecticut, Storrs, Connecticut 06269, USA; Tel.: +860-486-5523; fax: +860-486-2447.
  E-mail address: zhu@engr.uconn.edu (Q. Zhu).

[24–38]. Typically, to deliver light to the tissue, one or several optical fibers or fiber bundles are integrated with the ultrasound transducer. In the compact probe design for endoscopic and intravascular applications, single fibers with core diameters of a few to several hundred microns are utilized [24–27]. Due to the relatively small core area, the energy density of the coupled light at the fiber end face is high. In order not to damage the fiber, the available light energy at the end face is limited. As a result, these fibers are most suitable for imaging shallow lesions where the laser intensity required is relatively low. Fiber bundles on the other hand have the advantages of a relatively larger optically active areas and good mechanical flexibility and have been used in photoacoustic imaging probes [28–38]. However, their large diameter sizes make them unsuitable for transvaginal photo-acoustic/ultrasound probes. Another drawback is their high loss in light transmission, which potentially reduces the signal-to-noise ratio (SNR) of the detected photoacoustic signals. In our earlier study, we designed a transvaginal photoacoustic/ultrasound probe suitable for imaging of human ovaries [39]. This probe consisted of 36, 200-micron core fibers from a pair of custom-made high-power fiber-optic beamsplitter assembly integrated with the ultrasound transducer. Unfortunately, this specialty beamsplitter is rather expensive and moreover prone to damage at the fiber input end and the junction between the input and output fibers with repeated use, when a high intensity (>20 mJ/pulse) laser source is employed.

In this paper, we report the optimal design, implementation, and evaluation of an optical fiber-based transvaginal photoacoustic/ultrasound imaging probe with significantly improved light delivery efficiency, low-cost, robust operation for extended use as well as a homogeneous distribution of irradiance. The light delivery system consists of light coupling optics, a custom-made transducer sheath internally lined with highly reflecting aluminum sheet, and four 1-mm-core multi-mode optical fibers surrounding the ultrasound transducer. The transducer and fibers are housed inside the sheath, and the aluminum material lining serves as a light tunnel for high-efficiency light transmission. The probe design was optimized by simulating the light fluence and power output efficiency, and was further evaluated by experimental measurements.

2. Methods and Materials

2.1. Optimization of imaging probe design

The probe design was optimized to deliver good light uniformity on tissue surface, high power output efficiency, and acceptable fluence levels below the ANSI safety limit (25 mJ/cm^2 at 750 nm wavelength) [40]. The power output efficiency is defined as the ratio of the total energy output from the probe to the total energy exiting the four fibers. The optimization was performed by simulating the fluence distribution of the four fibers using a 3D model in Zemax. The model of the imaging probe [41], shown in Fig. 1, consisted of two concentric hollow cylinders and represented the transvaginal ultrasound transducer and the probe sheath respectively. For a more realistic geometry, the cross-sectional area of the first cylinder, representing the ultrasound transducer, was gradually tapered down to a radius of 5 mm. This shape resembled closely the actual transvaginal probe used in the experiments. The diameter of the inner cylinder was chosen as 20 mm - same as the diameter of the transducer used in the experiments. The diameter of the outer cylinder however was varied to obtain one that provides the best results, as will be explained in the subsequent sections. The illumination fibers were sandwiched between the two hollow cylinders. Additionally, the surfaces of the cylinders bordering the fibers were chosen to have a
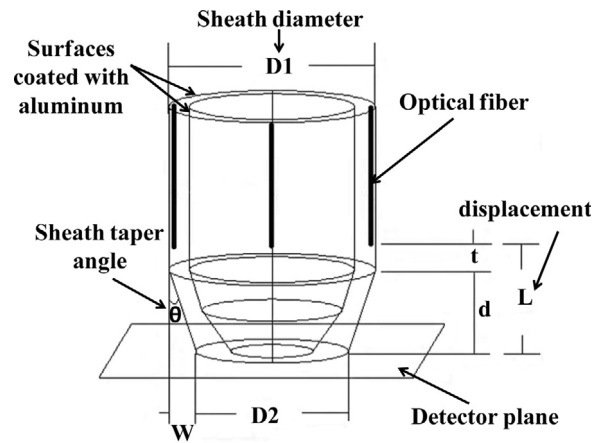

Fig. 1. The model of the imaging probe employed in the simulation with all the design parameters shown. L: fiber displacement, D1: probe diameter, and θ: sheath taper angle.

reflection coefficient of 85% at 750 nm, this is the same value as the reflection coefficient of the aluminum sheet that was used in the actual construction of the probe. The optical detection plane was chosen to be a plane parallel to the surface area of the probe base and just touching it (Fig. 1). In the simulation, a detector was placed at this plane to measure the laser fluence and power output efficiency. The fluence delivered to the tissue surface was calculated based on the incident optical energy and the illumination area.

Various parameters of the imaging probe were investigated in order to obtain acceptable fluence levels, while at the same time yielding high power output efficiencies. These parameters are: 1) fiber numerical aperture (NA); 2) fiber displacement from the probe base (L); 3) sheath diameter (D1); and 4) sheath taper angle (θ); for a definition of these terms, see Fig. 1.

Fiber numerical aperture and displacement from probe base (L): The first parameters that were investigated were the fiber numerical aperture and the longitudinal displacement (L) from the base of the probe. The angle of divergence of light exiting the fiber depends on the fiber's numerical aperture- higher numerical apertures yield greater divergences. Therefore, this numerical aperture effect was simulated in Zemax by adjusting the divergence of the light source to correspond to the fiber numerical aperture that would give the same divergence. The fiber numerical aperture was calculated by *sine (angle of divergence)*. The fiber displacement (L) was also accomplished in Zemax by changing the positions of the Gaussian light sources in the vertical direction. In all, four different numerical apertures, of values, 0.21, 0.36, 0.48, 0.65, and four displacements, 5, 10, 15, and 20 mm were simulated. For each displacement, the fluence and power output efficiency at the imaging plane were simulated for all the numerical aperture values and compared. The simulation results were obtained with the sheath diameter fixed at 25 mm and sheath taper angle at 0°. The distance t was not varied and its purpose was to provide some space for the fiber holder. Moreover, Monte Carlo (MC) simulation was performed to estimate light reflection events of photons at the surfaces with various numerical apertures. A 2D model was used for the simulation. After the photon was generated, it reflected between the two surfaces according to the law of reflection, until it reached the detector plane. The MC code was a custom program written by the authors.

Sheath diameter (D1) and taper angle (θ): The next parameters that were investigated were the sheath diameter and taper angle. Different sheath diameters were simulated simply by changing the diameter of the outer cylinder. Diameters of 23, 24, 25, and 26 mm

were investigated for the least fluence and highest power output efficiency. For each probe diameter, the sheath taper angle was varied for values of 0°, 1.78°, 3.57°, 5.35°, 7.12°, 8.88°, 10.62°, 12.34°, and 14°. These angles were simulated by fixing the value of d at 8 mm and changing W from 0.25 mm to 2 mm, and were simply calculated from the inverse tangent of the ratio W/d (See Fig. 1). The simulation results were obtained with a beam divergence corresponding to a fiber numerical aperture of 0.48, displacement of 10 mm.

2.2. Implementation of imaging probe

The imaging probe was constructed based on the optimal parameters that were obtained from the simulation. This construction consisted of four 1-mm-core optical fibers with numerical aperture of 0.48 that were conveniently integrated with a transvaginal ultrasound transducer, to deliver light to the imaged tissue. A custom-made light-weight sheath, made of acrylonitrile butadiene styrene (ABS) material and constructed with a 3D printer (the sheath surface was polished), encased the ultrasound transducer and optical fibers as shown in Fig. 2. The inner surface of the sheath and the outer surface of the ultrasound transducer were covered with an aluminum sheet having a reflection coefficient of 85% at 750 nm wavelength. This reflection coefficient was experimentally measured as the ratio of reflected light from the aluminum sheet to incident light. In addition to improving light output, this reflective material also served to homogenize the light output of the four fibers and eliminate any potential hotspots in the output beam profile that would result in a high fluence. Additionally, the sheath protects the fibers from getting broken and also getting too close to the tissue and causing injury during clinical studies. The sheath was designed to gradually taper towards the bottom end to allow for easy penetration into the body cavity. A pair of holding fixtures that go around the sheath and screw together allows it to be securely attached to the ultrasound transducer. During clinical studies, the probe will be covered by a transparent condom which is typically used in transvaginal examination of the ovaries. In this probe design, the light delivery setup is low-cost and not prone to be damaged with repeated use.

2.3. Experimental setup of photoacoustic/ultrasound imaging

The experimental setup of the photoacoustic/ultrasound imaging system is shown in Fig. 2(a). Light from the laser source was split into four equal beams and each beam coupled into one of the four fibers. The illumination fibers were affixed to a 128-element transvaginal ultrasound transducer array of 6 MHz central frequency and 80% bandwidth (W.L. Gore and Associates, Inc., Newark, DE). Furthermore, light was guided to the tissue surface by tunneling through the probe sheath that was internally lined with highly reflecting aluminum sheet, and the ultrasound transducer coated with the same reflecting aluminum material. The laser utilized was a tunable-wavelength Ti: Sapphire (Symphotics TII, LS-2211) optically pumped by a Q-switched Nd:YAG (Symphotics TII, LS-2134). It delivered 20 ns pulses at 15 Hz repetition rate with 20 mJ/pulse at the imaging wavelength of 750 nm. The data acquisition system was a 128-channel imaging system with real-time co-registration of the two modalities, which provides up to 15 coregistered frames per second limited by the laser pulse repetition rate [42]. Resolution measurements for pulse-echo ultrasound and photoacoustic modes were performed using a 100-μm diameter black nylon thread. To measure the lateral resolution of the system, the thread was placed in a water tank at a 30 mm depth with its orientation perpendicular to the imaging plane. The lateral profiles of pulse-echo US and PAT modes were measured and are shown in Fig. 2(b). The measured -6 dB full width at half maximum (FWHM) from the beam profiles of the thread was used to obtain the resolutions [20,42]. The FWHMs of lateral beam profiles were 1.5° in the US mode and 2° in the PAT mode.

2.4. Performance evaluation and ex vivo studies

The laser fluence distribution was experimentally measured on the tissue surface, through chicken breast tissue and calibrated intralipid solution (Fresenius Kabi) at different depths, with a CMOS camera (Edmund Optics USB EO-0413 M 1/3" CMOS Monochrome). The intralipid solution had a reduced scattering coefficient (μ'_s) of 4 cm^{-1} and absorption coefficient (μ_a) of 0.02 cm^{-1}. A fluence distribution was first captured on the tissue
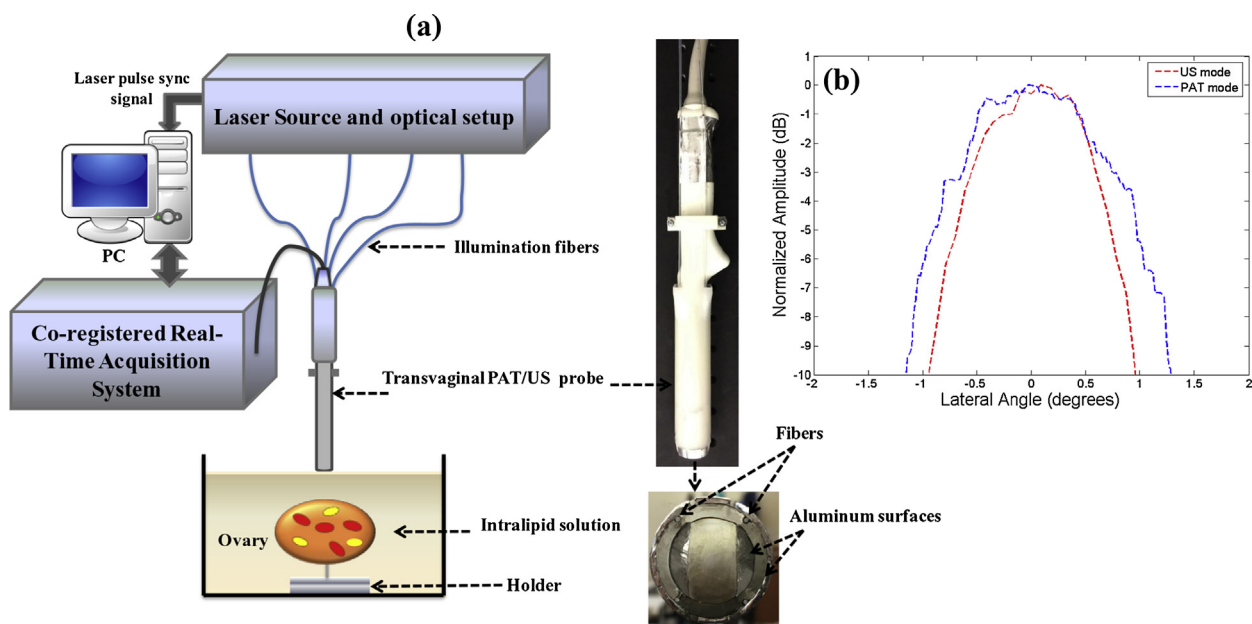

Fig. 2. (a) The experimental setup utilized to acquire the co-registered photoacoustic/ultrasound images. (b) Lateral profiles of US and PAT modes measured from a 100 μm black thread.
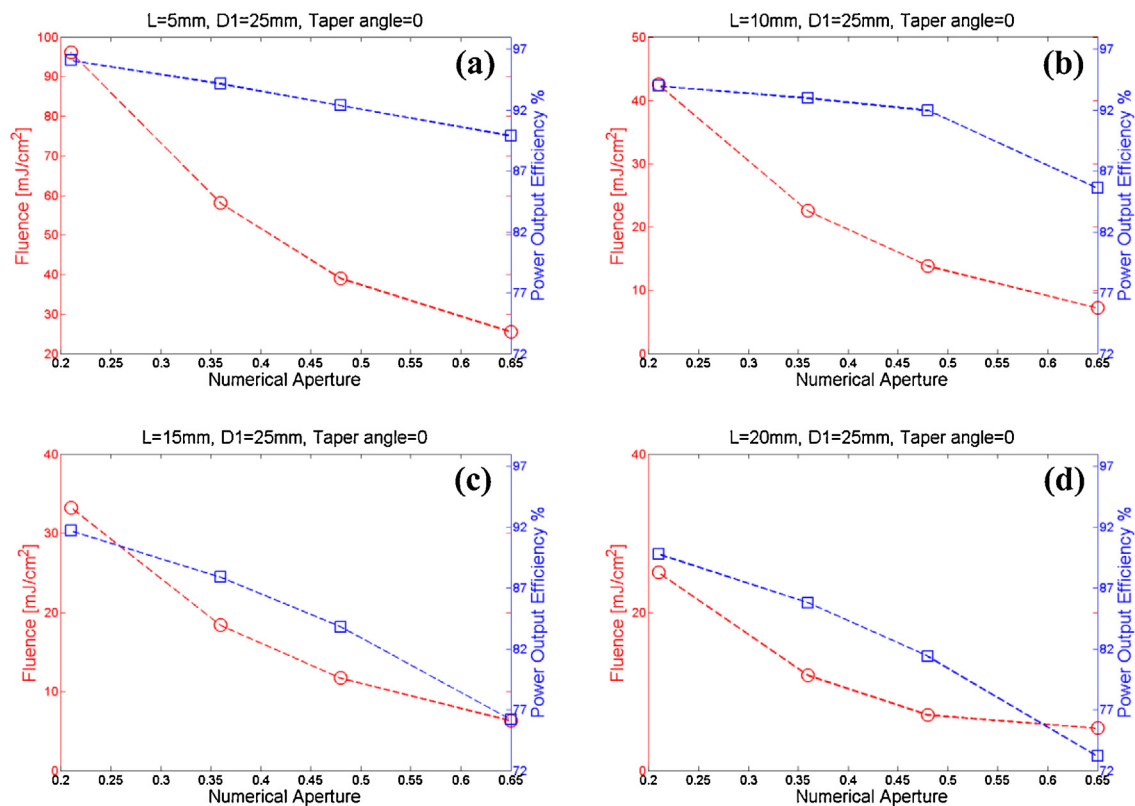
Fig. 3. The fluence and power output efficiency for fibers having different numerical apertures (NA of 0.21, 0.36, 0.48, and 0.65) and displacements from the probe base: (a) displacements of 5 mm, (b) displacements of 10 mm, (c) displacements of 15 mm, (d) displacements of 20 mm.

surface, then through 10 mm chicken tissue, and lastly through the chicken tissue that was directly placed above a column of the intralipid solution; different thicknesses of the intralipid column varying from 5 mm to 15 mm were used. In another set of experiments, a 0.86mm-inner-diameter polyethylene tubing (Intramedic Polyethylene Tubing, Becton Dickinson (BD)) filled with rat blood mimicking a blood vessel was immersed in intralipid solution and imaged from depths of ~12 mm up to ~30 mm through porcine vaginal tissue with thickness of ~8 mm by using 750 nm wavelength. This imaging depth was achieved using a laser fluence on the tissue surface of 20 mJ/cm², which is below the ANSI safety limit (25 mJ/cm² at 750 nm). Normal clotting time is between 2 to 6 minutes, which is enough time for our real-time imaging system to image the blood before coagulation.

Human ovaries were obtained from patients undergoing prophylactic oophorectomy at the University of Connecticut Health Center (UCHC). These patients were at risk for ovarian cancer or they had ovarian mass or pelvic mass suggesting malignancy. This study was approved by the Institutional Review Boards of the UCHC, and informed consent was obtained from all patients. Ovaries were kept in the 0.9% wt/vol NaCl solution and imaged within 24 hours after oophorectomy. During *ex vivo* imaging, human ovary was immersed in the intralipid solution with μ_a of 0.02 cm^{-1} and μ'_s of 4 cm^{-1}. Each ovary was mounted on a supporting frame made of a transparent thin optical fiber net and immersed inside a calibrated intralipid solution tank. The distance between the sample and the imaging probe surface was adjusted to approximately 10 mm. In general, most ovaries are expected to be imaged *in vivo* at depth of ~8 to 10 mm- the thickness of human vaginal muscle wall. This muscle wall, being the intervening structure between the imaging probe and the ovary, will absorb and scatter some of the light. The ovaries were

imaged with an average of 32 laser pulses, 50 dB US dynamic range and 15 dB PAT dynamic range. After photoacoustic/ultrasound imaging, the ovaries were fixed in 10% formalin solution and returned to the Pathology Department for histological processing.

3. Results

3.1. Simulation results

Fiber numerical aperture and displacement (L): The effects of using different fiber numerical apertures and displacements on the light fluence and power output efficiency are shown in Fig. 3. It is seen that at each of the displacement L, as the numerical aperture increases both the power output efficiency and fluence decrease. This can be explained by the increasing divergence of the light exiting the fiber, which in turn increases light reflection events of photons and results in more homogenized beam.

The Monte Carlo simulation shows that for the numerical aperture of 0.65, 50.34% of the photons experienced multiple reflections (two or more), 31.66% of the photons experienced one reflection, and 18% of the photons reached the detector plane directly without any reflection, as shown in Table 1. On the other hand, the numerical aperture of 0.21 shows only 32.95% of the photons undergoing multiple reflections, 42.66% of the photons experienced one reflection, and 24.39% of the photons reached the detector plane directly. A greater numerical aperture increases the number of multiple reflections, consequently decreasing the efficiency. However, the photon multiple reflections homogenize the light distribution of the four fibers on the tissue surface and eliminate any potential hotspots.

Ultimately, the choice of the optimal fiber numerical aperture and displacement L comes down to the level of fluence that can be

Table 1
The Monte Carlo simulation for light reflection events of photons with various numerical apertures.

Numerical Aperture	No Reflection %	One Reflection %	Two Reflections or more %
0.21	24.39	42.66	32.95
0.36	20.82	37.54	41.61
0.48	19.33	34.71	45.96
0.65	18	31.66	50.34

tolerated in the imaging environment. If the fluence threshold that can be tolerated by the tissue is high, then probes can be designed that have higher output efficiencies. In our work for example, the ovary images were acquired at a wavelength of 750 nm with a total of ~20 mJ/pulse exiting the four fibers. According to ANSI, at this wavelength, the MPE should not exceed 25 mJ/cm^2. Therefore, we chose a fiber numerical aperture of 0.48 and displacement L of 10 mm as the optimal parameters (with fluence of ~14 mJ/cm^2 and efficiency of ~92%, as shown in Fig. 3(b)). Although numerical aperture of 0.36 and L of 10 mm (Fig. 3(b)) provides better power output efficiency, the fluence could exceed the MPE even with small laser intensity fluctuations. The choice of L = 15 mm and NA = 0.36 provides less power output efficiency of ~88% (Fig. 3(c)), whereas the choice of L = 10 mm and NA = 0.48 provides ~92% efficiency (4% more). Fig. 4(a) and 4(b) illustrate the fluence profiles on the tissue surface and at the imaging depth of 10 mm within the tissue. Transvaginal imaging of ovaries requires light to first penetrate through vaginal muscle wall before reaching the ovary. Consequently, the scattering medium was modeled as a vaginal muscle wall of 1 cm thickness with absorption coefficient of μ_a=0.02 cm^{-1}, reduced scattering coefficient of μ'_s=4 cm^{-1}, and transport mean free path distance of $l'_t = \frac{1}{\mu_a + \mu'_s} = 2.48$mm. Note that, the fluence was homogenized after propagating in vaginal muscle wall. Fig. 4(c) shows the 1D fluence profile at the same depth. These profiles were obtained using 10 mm fiber displacement (L) and numerical aperture of 0.48.

Sheath diameter (D1) and taper angle (θ): The effects of the sheath diameter and taper angle on the probe's performance are

shown in Fig. 5. As the probe diameter increases, the power output efficiency also increases. It should be noted that for larger sheath diameters, the transducer and sheath surfaces sandwiching the fibers are further apart, and hence the number of photons reflected off from them is decreased. Thus, the larger the sheath diameter, the better the probe performance in terms of output efficiency. With regard to patient comfort however, the larger physical sheath diameter becomes a drawback. In this case therefore, there is a tradeoff between patient comfort and high fluence with low output efficiency. The suboptimal sheath diameter that we have used for our sheath design and implementation is 25 mm, as it provides a fairly acceptable size, and high output efficiency, as well as fluence level below the MPE.

Another observation that can readily be deduced from Fig. 5 is the effects of the taper angle on the probe performance. As the taper angle increases, the power output efficiency decreases. The main reason for this is that part of the light is back reflected and scattered due to the taper angles. Fig. 5(c) shows that with the sheath diameter of 25 mm, taper angle values of 5.35o and 8.88o have either high fluence or low power output efficiency compared to taper angle 0o which has fluence of ~14 mJ/cm2 and efficiency of ~92%. Therefore, the suboptimal sheath taper angle implemented in our design is 7.12o and provides reasonable power output efficiency and fluence with acceptable tapered head (fluence of ~17 mJ/cm2 and efficiency of ~89%).

3.2. Experimental results

The optical coupling efficiency of the optical fibers was determined from the ratio of the measured total energy output from the four fibers to the total energy incident at their input end faces, and was ~84%. The power output efficiency, defined as the ratio of the total energy output from the probe to the total energy exiting the four fibers, had an experimental value of ~88%. The overall efficiency of the light delivery system is the multiplication of the optical coupling efficiency and the power output efficiency, which is ~74%.

Fig. 6(a) demonstrates the experimental fluence distribution on the tissue surface. The fluence spatial profile shown in Fig. 6(b) was measured after light propagated through 10 mm chicken breast
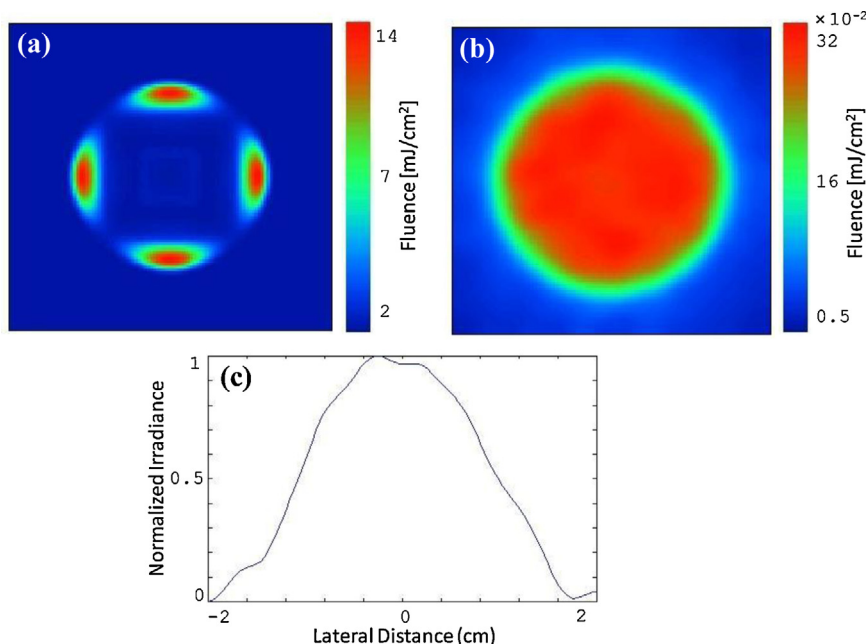

Fig. 4. The simulated fluence profile (a) on the tissue surface, and (b) through 10 mm tissue. (c) The 1D fluence profile along the middle section of image (b).
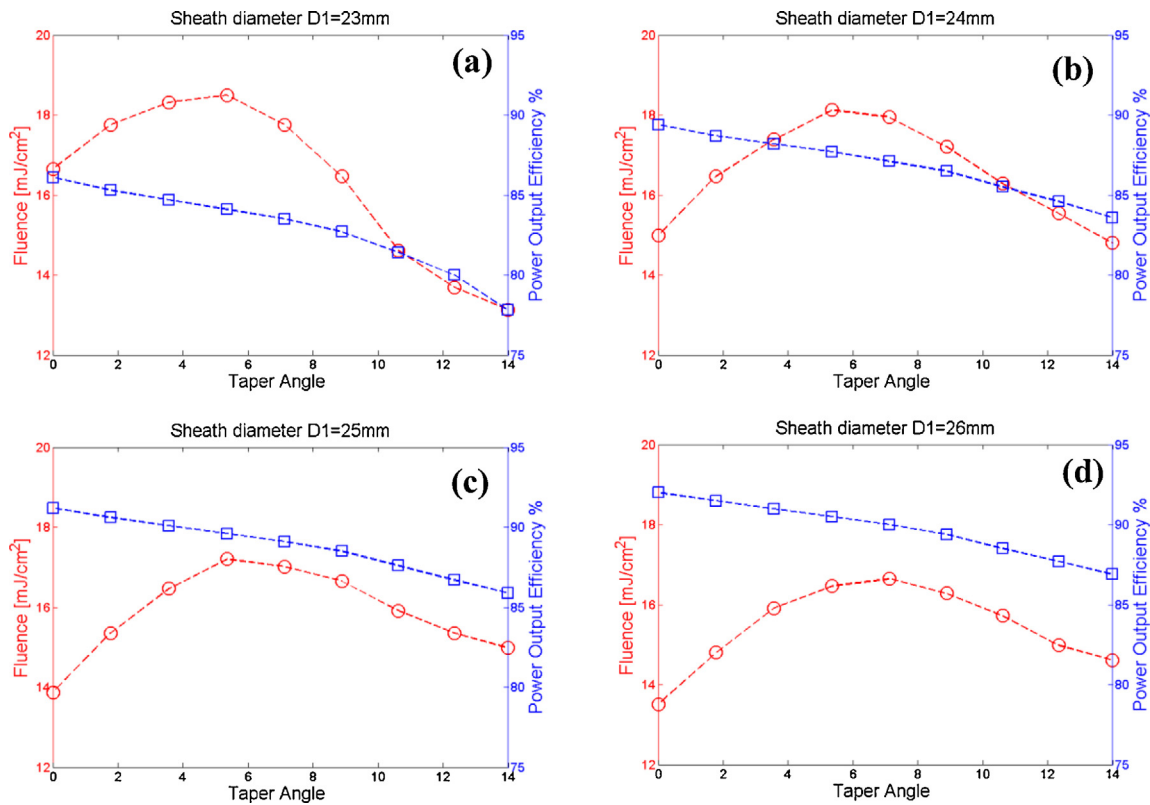
Fig. 5. The laser fluence and power output efficiency are shown for various taper angles: (a) sheath diameter (D1) of 23 mm, (b) D1 of 24 mm, (c) D1 of 25 mm, (d) D1 of 26 mm.

only. Similarly, the fluence profiles obtained through 10 mm chicken tissue with 5, 10, and 15 mm thickness intralipid solution below the chicken layer. Fig. 6(c) shows the corresponding 1D profiles of the fluence along the horizontal direction in Fig. 6(b). These plots show that the fluence at shallower depths are higher in
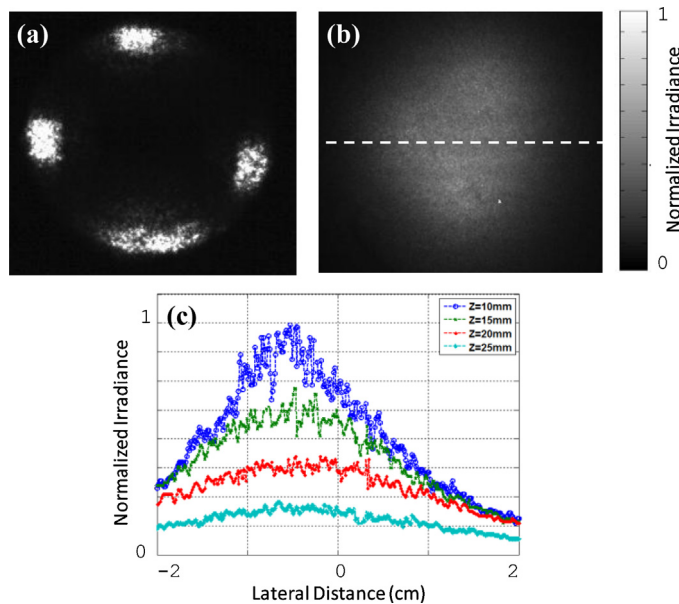

Fig. 6. The experimental laser fluence profiles on the tissue surface, through the chicken breast tissue and calibrated intralipid solution. (a) The laser fluence profile on the tissue surface. (b) The fluence profile pattern through 10 mm chicken tissue. (c) The corresponding 1D profile taken along the middle intersection in the horizontal direction at different depths (z of 10, 15, 20, and 25 mm).

intensity, as expected. At z = 10 mm, which is the depth at which most human ovaries are expected to be imaged *in vivo*, the fluence is fairly uniform with a full width at half maximum (FWHM) of ~20 mm.

Fig. 7 shows co-registered photoacoustic/ultrasound images of a polyethylene tube filled with rat blood that was imaged through a ~8 mm porcine vaginal tissue. Intralipid of 4 cm^{-1} reduced scattering coefficient, mimicking the scattering property of the tissue, was used for ultrasound coupling. The gray scale image is the ultrasound pulse-echo, and the color superimposed on gray scale image is the photoacoustic image. Fig. 7(a) and 7(b) clearly show the front and back of the blood-filled tube at imaging depths of (a) ~12 mm and (b) ~30 mm. In Fig. 7(a), the SNR was 22.5 dB, and at the ~30 mm depth, the SNR was 13.2 dB. The SNR is defined as the mean of photoacoustic signals obtained from the phantom target divided by the background noise measured at the region with no light illumination. The images were acquired at 750 nm wavelength with a fluence of 20 mJ/cm^2 on the tissue surface. This value is below the MPE of 25 mJ/cm^2 recommended by ANSI, suggesting the potential of the imaging probe to image through vaginal tissue in clinical studies.

The probe imaging capability was also verified with *ex vivo* imaging of benign and malignant human ovaries. Fig. 8(a) shows a co-registered photoacoustic/ultrasound image of a benign ovary from a 52-year-old premenopausal patient. In the ultrasound image, the only feature that stands out is a cyst that is about 10 mm in diameter. However, photoacoustic imaging reveals the presence of vascularity around the cyst. Fig. 8(b) shows a photograph of the benign ovary. Hematoxylin and eosin (H&E) staining of the corresponding histological slide as illustrated in Figs 8(c) and 8(d), shows excellent agreement with the cyst seen by ultrasound and the microvessels (black arrows in Fig. 8(d)) seen by
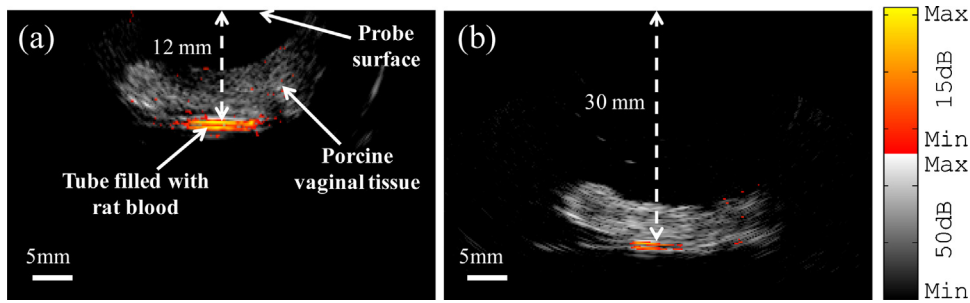
Fig. 7. Co-registered photoacoustic/ultrasound images of the polyethylene tubing filled with rat blood and placed under porcine vaginal tissue with thickness of ~8 mm, (a) at imaging depth of ~12 mm, (b) at imaging depth of ~30 mm.
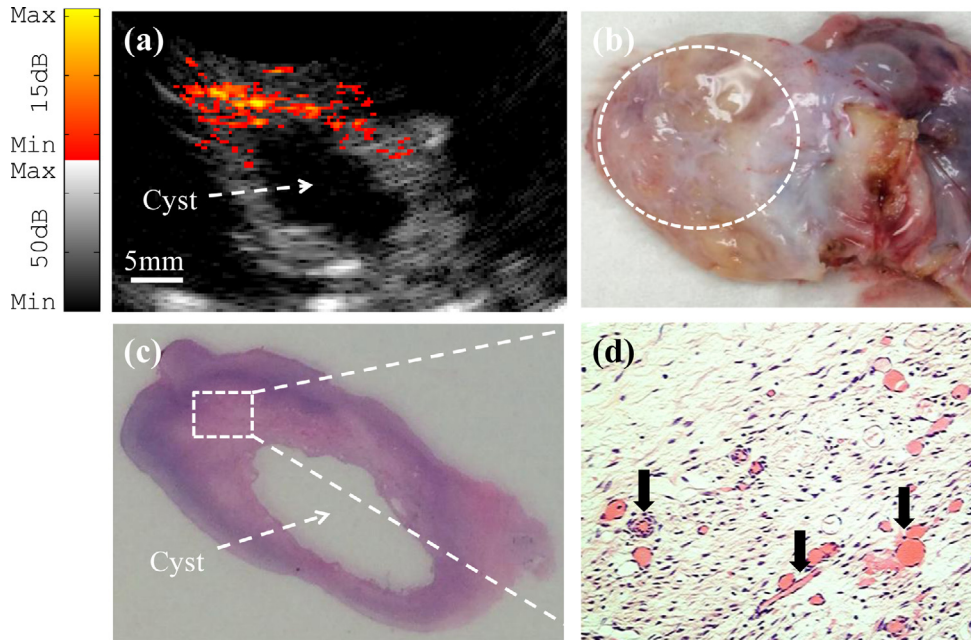

Fig. 8. (a) *Ex vivo* co-registered photoacoustic/ultrasound image of premenopausal ovary with benign tissue. (b) Photograph of the benign ovary with a dashed circle pointing to the ROI. (c) H&E staining of the corresponding area (×1); (d) Reveals microvessels from the rectangular region indicated in (c) (×40).

photoacoustic imaging. The SNR obtained from the photoacoustic image was 23.2 dB. A co-registered photoacoustic/ultrasound image of a malignant ovary from a 68-year-old postmenopausal woman is shown in Fig. 9(a). The photoacoustic image reveals a highly vascularized surface area compared with the surrounding tissue. Fig. 9(b) shows a photograph of the malignant ovary. Histologic evaluation of the sample reveals clusters of small vessels and malignant cancer cells on the surface of the ovary as shown in Fig. 9(c). Note that, up to 85% to ~ 90% of ovarian cancers are epithelial ovarian carcinomas located at the outer surface of the
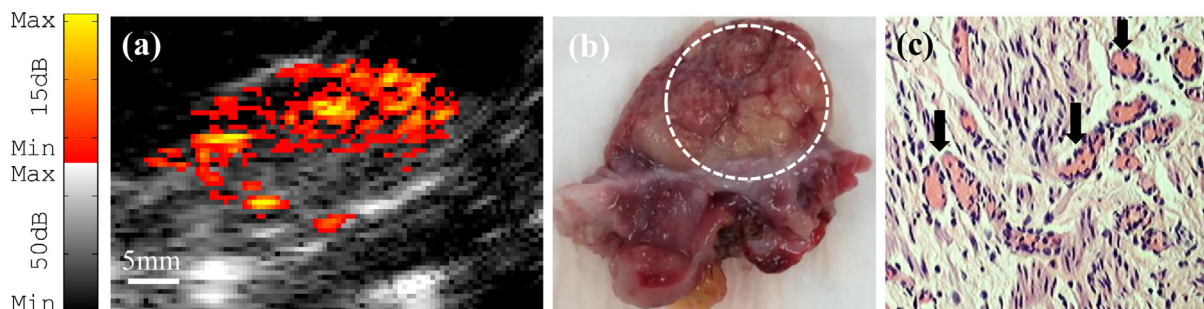

Fig. 9. (a) *Ex vivo* co-registered photoacoustic/ultrasound image of a postmenopausal ovary with malignancy. (b) Photograph of the malignant ovary with a dashed circle pointing to the ROI. (c) H&E staining of the sample reveals clusters of microvessels (×40).

ovaries [43]. For this image, the SNR obtained for the photoacoustic image was 25.3 dB.

4. Discussion

The goal of this research is to design, optimize, implement, and evaluate a transvaginal photoacoustic/ultrasound probe for clinical studies. Therefore, it is important to have a trade-off of the design parameters, such as laser fluence level on the tissue surface, uniformity of the fluence distribution, light output efficiency of the probe for improved tissue penetration, diameter of the probe, and clinical operation. Although our design is targeted for transvaginal co-registered photoacoustic/ultrasound imaging, the design principle is applicable to other endoscopic probe designs and applications such as optical coherence tomography- ultrasound-photoacoustic (OCT-US-PA) endoscopic probes for ovarian and prostate cancers.

Two important parameters affect the light penetration in tissue. One is the light output efficiency of the probe for a given power at the fiber tip, and another is the fluence on the tissue surface. It is desirable to have high probe output efficiency so the SNR of the image can be improved. On the other hand, the fluence on the tissue surface has to be kept under the MPE for patient safety. Therefore, the light output beam needs to be homogenized to keep high probe output efficiency and acceptable fluence that is under the MPE. A homogenized beam pattern also provides more uniform target illumination, especially when the target is located near the probe. The simulations have shown that the light beam from a point source is homogenized after propagating in vaginal muscle wall for about 10 mm in depth.

Lastly, in the reported studies, the highly reflecting aluminum sheet was used as the internal lining material because it is low cost and readily available. Silver foil can provide higher power output efficiency. Based on Ref. [44], the reflectance of aluminum (Al) and silver (Ag) are ~90% and ~97% respectively. In future studies, silver foil will be considered as the internal lining material to further increase the light coupling efficiency while keeping the fluence under the ANSI safety limit.

5. Conclusion

A hand-held transvaginal photoacoustic/ultrasound probe for noninvasive imaging of human ovaries has been demonstrated. The high optical power output efficiency, uniform fluence distribution, small probe diameter, as well as the safe energy levels (below the ANSI safety limit), make the designed probe suitable for *in vivo* noninvasive evaluation of ovarian tissue and early cancer detection.

Conflict of interest

The authors declare that there is no conflict of interest.

Acknowledgments

References

[1] D.L. Clarke-Pearson, Screening for Ovarian Cancer, N Engl J Med 361 (2009) 170–177.

[2] K.N. Danforth, T.M. Im, E.P. Whitlock, Addendum to Screening for Ovarian Cancer, Evidence Update for the U.S. Preventive Services Task Force Reaffirmation Recommendation Statement 4 (2012) 12–05165.

[3] D.A. Fishman, L. Cohen, S.V. Blank, L. Shulman, D. Singh, K. Bozorgi, R. Tamura, I. Timor-Tritsch, P.E. Schwartz, The role of ultrasound evaluation in the detection of early-stage epithelial ovarian cancer, Am J Obstet Gynecol 192 (2005) 1214–1222.

[4] K.H. Lu, S. Skates, M.A. Hernandez, D. Bedi, T. Bevers, L. Leeds, et al., A 2-stage ovarian cancer screening strategy using the Risk of Ovarian Cancer Algorithm (ROCA) identifies early-stage incident cancers and demonstrates high positive predictive value, Cancer 119 (2013) 3454–3461.

[5] J. Tammela, S. Lele, New modalities in detection of recurrent ovarian cancer, Curr Opin Obstet Gynecol 16 (2004) 5–9.

[6] V. Nossov, M. Amneus, F. Su, J. Lang, J.M. Janco, S.T. Reddy, R. Farias-Eisner, The early detection of ovarian cancer: from traditional methods to proteomics, Can we really do better than serum CA-125. Am J Obstet Gynecol 199 (2008) 215–223.

[7] B.V. Calster, D. Timmerman, T. Bourne, A.C. Testa, C.V. Holsbeke, E. Domali, D. Jurkovic, P. Neven, S.V. Huffel, L. Valentin, Discrimination Between Benign and Malignant Adnexal Masses by Specialist Ultrasound Examination Versus Serum CA-125, J Natl Cancer Inst 99 (2007) 1706–1714.

[8] M. Goozner, Personalizing ovarian cancer screening, J Natl Cancer Inst 102 (2010) 1112–1113.

[9] J.R. Nagell, P.D. DePriest, F.R. Ueland, C.P. DeSimone, A.L. Cooper, J.M. McDonald, E.J. Pavlik, R.J. Kryscio, Ovarian cancer screening with annual transvaginal sonography: findings of 25,000 women screened, Cancer 109 (2007) 1887–1896.

[10] A.A. Oraevsky, R.O. Esenaliev, S.L. Jacques, S.L. Thomsen, F.K. Tittel, Lateral and z-axial resolution in laser optoacoustic imaging with ultrasonic transducers, Proc SPIE 2389 (1995) 198–208.

[11] V.G. Andreev, A.A. Karabutov, A.A. Oraevsky, Detection of ultrawide-band ultrasound pulses in optoacoustic tomography, IEEE Trans Ultrason Ferroelectr Freq Control 50 (2003) 1383–1390.

[12] X. Wang, Y. Pang, G. Ku, X. Xie, G. Stoica, L.V. Wang, Noninvasive laser-induced photoacoustic tomography for structural and functional in vivo imaging of the brain, Nat Biotechnol 21 (2003) 803–806.

[13] B.T. Cox, P.C. Beard, Fast calculation of pulsed photoacoustic fields in fluids using k-space methods, J Acoust Soc Am 117 (2005) 3616–3627.

[14] A. Karabutov, E.V. Savateeva, N.B. Podymova, A.A. Oraevsky, Backward mode detection of laser-induced wide-band ultrasonic transients with optoacoustic transducer, J Appl Phys 87 (2000) 2003–2014.

[15] G. Ku, X. Wang, G. Stoica, L.V. Wang, Multiple-bandwidth photoacoustic tomography, Phys Med Biol 49 (2004) 1329–1338.

[16] G. Paltauf, J.A. Viator, S.A. Prahl, S.L. Jacques, Iterative reconstruction algorithm for optoacoustic imaging, J Acoust Soc Am 112 (2002) 1536–1544.

[17] S. Sethuraman, J.H. Amirian, S.H. Litovsky, R.W. Smalling, S.Y. Emelianov, Spectroscopic intravascular photoacoustic imaging to differentiate atherosclerotic plaques, Opt Express 16 (2008) 3362–3367.

[18] J. Laufer, P. Johnson, E. Zhang, B. Treeby, B. Cox, P. Pedley, P. Beard, In vivo preclinical photoacoustic imaging of tumor vasculature development and therapy, J Biomed Opt 17 (2012) 056016.

[19] J. Gamelin, A. Aguirre, A. Maurudis, F. Huang, D. Castillo, L.V. Wang, Q. Zhu, Curved array photoacoustic tomographic system for small animal imaging, J Biomed Opt 13 (2008) 024007.

[20] A. Aguirre, P. Guo, J. Gamelin, S. Yan, M.M. Sanders, M. Brewer, Q. Zhu, Coregistered three-dimensional ultrasound and photoacoustic imaging system for ovarian tissue characterization, J Biomed Opt 14 (2009) 054014.

[21] A. Aguirre, Y. Ardeshirpour, M.M. Sanders, M. Brewer, Q. Zhu, Potential Role of Coregistered Photoacoustic and Ultrasound Imaging in Ovarian Cancer Detection and Characterization, Trans Oncology 4 (2011) 29–37.

[22] J.J. Niederhauser, M. Jaeger, R. Lemor, P. Weber, Combined ultrasound and optoacoustic system for real-time high-contrast vascular imaging in vivo, IEEE Trans Med Imaging 24 (2005) 436–440.

[23] J. Folkman, Role of angiogenesis in tumor growth and metastasis, Semin Oncol 29 (2002) 15–18.

[24] B. Wang, J.L. Su, A.B. Karpiouk, K.V. Sokolov, R.W. Smalling, S.Y. Emelianov, Intravascular Photoacoustic Imaging, IEEE J Sel Top Quantum Electron 16 (2010) 588–599.

[25] J.M. Yang, R. Chen, C. Favazza, J. Yao, C. Li, Z. Hu, Q. Zhou, K.K. Shung, L.V. Wang, A 2.5-mm diameter probe for photoacoustic and ultrasonic endoscopy, Opt Express 20 (2012) 23944–23953.

[26] J.A. Viator, B. Choi, M. Ambrose, J. Spanier, J.S. Nelson, In vivo port-wine stain depth determination with a photoacoustic probe, Appl Opt 42 (2003) 3215–3224.

[27] L. Song, K. Maslov, K.K. Shung, L.V. Wang, Ultrasound-array-based real-time photoacoustic microscopy of human pulsatile dynamics in vivo, J Biomed Opt 15 (2010) 021303.

[28] T.J. Allen, P.C. Beard, Pulsed near-infrared laser diode excitation system for biomedical photoacoustic imaging, Opt Lett 31 (2006) 3462–3464.

[29] C. Kim, T.N. Erpelding, L. Jankovic, L.V. Wang, Performance benchmarks of an array-based hand-held photoacoustic probe adapted from a clinical ultrasound system for non-invasive sentinel lymph node imaging, Philos Trans A Math Phys Eng Sci 369 (2011) 4644–4650.

[30] S. Mallidi, T. Larson, J. Tam, P.P. Joshi, A. Karpiouk, K. Sokolov, S. Emelianov, Multiwavelength photoacoustic imaging and plasmon resonance coupling of

gold nanoparticles for selective detection of cancer, Nano Lett 9 (2009) 2825–2831.

[31] J. Dean, V. Gornstein, M. Burcher, L. Jankovic, Real-time photoacoustic data acquisition with Philips iU22 ultrasound scanner, Proc SPIE 6856 (2008) 685622–685631.

[32] C. Kim, T.N. Erpelding, L. Jankovic, M.D. Pashley, L.V. Wang, Deeply penetrating in vivo photoacoustic imaging using a clinical ultrasound array system, Biomed Opt Express 1 (2010) 278–284.

[33] M.A. Yaseen, H.P. Brecht, S.A. Ermilov, R.R. Gharieb, A. Conjusteau, A. Oraevsky, Hybrid optoacoustic and ultrasonic imaging system for detection of prostate malignancies, Proc SPIE 6856 (2008), 68560T-1-11.

[34] A. Agarwal, S.W. Huang, M. O'Donnell, K.C. Day, M. Day, N. Kotov, S. Ashkenazi, Targeted gold nanorod contrast agent for prostate cancer detection by photoacoustic imaging, J Appl Phys 102 (2007), 064701-1-4.

[35] M.P. Patterson, M.G. Arsenault, C. Riley, M. Kolios, W.M. Whelan, Optoacoustic imaging of an animal model of prostate cancer, Proc SPIE 7564 (2010), 75641B-1-5.

[36] S.A. Ermilov, M.P. Fronheiser, H.P. Brecht, R. Su, A. Conjusteau, K. Mehta, P. Otto, A.A. Oraevsky, Development of Laser Optoacoustic and Ultrasonic Imaging System for breast cancer utilizing handheld array probes, Proc SPIE 7177 (2009), 717703-1-10.

[37] C. Haisch, K. Zell, J.I. Sperl, S. Ketzer, M.W. Vogel, P. Menzenbach, R. Niessner, Optoacoustic imaging combined with conventional ultrasound for breast cancer detection, Proc SPIE-OSA BioMed Opt 6631 (2007), 663105-1-14.

[38] M. Jaeger, S. Preisser, M. Kitz, D. Ferrara, S. Senegas, D. Schweizer, M. Frenz, Improved contrast deep optoacoustic imaging using displacement-compensated averaging: breast tumour phantom studies, Phys Med Biol 56 (2011) 5889–5891.

[39] P.D. Kumavor, U. Alqasemi, B. Tavakoli, H. Li, Y. Yang, X. Sun, E. Warych, Q. Zhu, Co-registered pulse-echo/photoacoustic transvaginal probe for real time imaging of ovarian tissue, J Biophotonics 6 (2013) 475–484.

[40] American National Standard for the Safe Use of Lasers, ANSI., Z136 (Laser Institute of America, Orlando, Florida 2007 1- 2007

[41] H.S. Salehi, P.D. Kumavor, U. Alqasemi, H. Li, T. Wang, Q. Zhu, High-throughput fiber-array transvaginal ultrasound/photoacoustic probe for ovarian cancer imaging, Proc. SPIE 8943 (2014) 894335.

[42] U. Alqasemi, H. Li, G. Yuan, P.D. Kumavor, S. Zanganeh, Q. Zhu, Interlaced photoacoustic and ultrasound imaging system with real-time coregistration for ovarian tissue characterization, J Biomed Opt 19 (2014) 076020.

[43] http://www.cancer.net/cancer-types/ovarian-cancer.

[44] Bates SC. Low Mass, Low Power, Low Cost Space Furnace. Thoughtventions Unlimited LLC, Glastonbury, CT: http://www.tvu.com/PLowPowerFurnaceWeb.html.
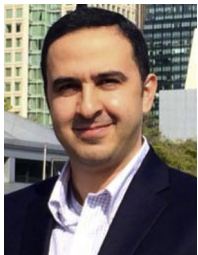
Hassan S. Salehi received his B.S. and M.E. degrees in Electrical Engineering. He is currently pursuing his Ph.D. in Optical and Ultrasound Imaging Lab at the University of Connecticut. His research interests include design and development of novel photoacoustic imaging systems and diffuse optical tomography for ovarian and breast cancers detection. Salehi is President of the Optical Society of America (OSA) UCONN Student Chapter, and he also served as the 2013-2014 President of the International Society for Optics and Photonics (SPIE) UCONN Student Chapter.


Patrick Kumavor holds a Ph.D. degree (electrical engineering) from the University of Connecticut (UConn). He also has an M.S. (biomedical engineering) and B.S. (physics). Patrick's area of specialization is optical signal processing where he has a plethora of research accomplishments ranging from high-speed signal processors, through quantum communications to biomedical imaging. Patrick is currently with the Biomedical Engineering Department at UConn. His most recent research work is the development of photoacoustic imaging techniques for ovarian cancer.

Hai Li received his B.S. degree and M.S degree in Biomedical Engineering from Xi'an Jiaotong University at Shaanxi, China in 2006 and 2009 respectively. He is a Ph.D. student in Electrical and Computer Engineering of University of Connecticut, Storrs, USA. He is working on the software design and implement for ultrasound and photoacoustic imaging system, digital signal processing and simulation for photoacoustic imaging of ovarian cancer diagnosis.

Umar Salman Alqasemi received B.Sc. degree in Electrical and Computer Engineering (Biomedical Engineering minor) from King Abdulaziz University – Jeddah, Saudi Arabia in 2007. Afterwards, he received M.Sc. and Ph.D. degrees in Biomedical Engineering from the University of Connecticut – Storrs, CT, USA in 2011 and 2013, respectively. He is serving as an assistant professor in the Dept. of Electrical and Computer Engineering at King Abdulaziz University since January 2014.
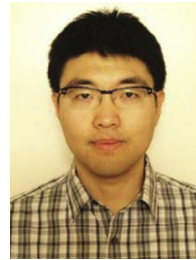
Tianheng Wang received his Ph.D. degree in Electrical Engineering from Optical and Ultrasound Imaging Lab at University of Connecticut in 2014. He received his B.S. and M.S. degrees from National Key Laboratory of Tunable Laser Technology at Harbin Institute of Technology, China in 2007 and 2009, respectively. He is the author of more than 20 peer-reviewed journal articles. His research interests include optical coherence tomography, photoacoustic imaging, optical microscopy, and solid-state lasers.

Chen Xu, Ph.D., is a Research Associate at the Electrical and Computer Engineering Department, University of Connecticut. She received her B.S. in Applied Physics and M.S degrees in Optics from Northwestern Polytechnical University, China, and Ph.D. degree in Biomedical Engineering at the University of Connecticut. Her research interests include the near-infrared diffusive tomography, photoacoustic tomography, light propagation in the scattered medium, Monte Carlo modeling, imaging reconstruction algorithms, breast cancer imaging and diagnosis.

Quing (Ching) Zhu received her Ph.D degree from the Bioengineering Department of the University of Pennsylvania in 1992 and she is currently a Professor in the Departments of Electrical & Computer Engineering and Biomedical Engineering of the University of Connecticut. Professor Zhu's research has focused on the development of novel imaging devices and algorithms using ultrasound and diffused light, ultrasound and photoacoustic imaging, nuclear detection and Optical Coherent Tomography for breast and ovarian cancer detection and diagnosis. She has published over 100 journal articles and numerous conference papers with her graduate students and postdoctoral fellows. She is a Fellow of SPIE International Society for Optics and Photonics.